

Micro Scale Laser Shock Processing of Metallic Components

Wenwu Zhang

Y. Lawrence Yao

Department of Mechanical Engineering,
Columbia University, New York, NY 10027

Laser shock processing of copper using focused laser beam size about ten microns is investigated for its feasibility and capability to impart desirable residual stress distributions into the target material in order to improve the fatigue life of the material. Shock pressure and strain/stress are properly modeled to reflect the micro scale involved, and the high strain rate and ultrahigh pressure involved. Numerical solutions of the model are experimentally validated in terms of the geometry of the shock-generated plastic deformation on target material surfaces as well as the average in-depth strains under various conditions. The residual stress distributions can be further influenced by shocking at different locations with certain spacing. The potential of applying the technique to micro components, such as micro gears fabricated using MEMS is demonstrated. The investigation also lays groundwork for possible combination of the micro scale laser shock processing with laser micromachining processes to offset the undesirable residual stress often induced by such machining processes. [DOI: 10.1115/1.1445149]

1 Introduction

Laser shock processing (LSP) has been studied since the 1960s [1–3]. Laser generated shock waves in a confining medium have been used to improve the mechanical properties of various metals such as aluminum, steel and copper. In particular, LSP can induce compressive residual stresses in the target and improve its fatigue life. The beam spot size used is in the order of millimeters and the compressive stress can typically reach a couple of millimeters into the target material. The technique has not been widely applied partially due to the fact that a high power laser source is needed for a beam size in the order of a millimeter to produce the high laser intensity required. It is also perceived as inefficient when a large area of surface needs to be processed because each laser pulse only processes a small area.

In recent decades, significant progress has been made in the design and fabrication of micro electromechanical systems (MEMS) via various methods. Failure and reliability of MEMS has been drawing increasing attention [4,5]. Some MEMS structures experience cyclic loadings in operation, such as microengines and micro-switches. Metals such as copper, nickel and aluminum are at times used in such structures due to their better mechanical and electrical properties compared with silicon. Fatigue and wearing are important failure modes for such structures. Needs will arise to impart a desirable residual stress distribution or alter the existing distribution left by the fabrication process itself. LSP can increase the hardness of metallic surfaces and thus improve the wearing resistance of the component. Microscale LSP can also alter the residual stress distribution thus improving the fatigue life of metal MEMS components. Little research has been done for such methods in the micro scale.

This paper investigates laser shock processing of copper with the laser beam size about ten microns. Simulation and experiments were carried out to determine the feasibility and capability of LSP at the micro scale. Simulation models were properly modified for the micro scale and LSP induced deformation was measured and used to validate the simulation model. The investigation is also aimed at laying groundwork for a possible combination of laser shock processing with laser micromachining processes.

2 Laser Shock Processing (LSP)

When a metallic target is irradiated by an intense ($>1 \text{ GW/cm}^2$) laser pulse, the surface layer instantaneously vaporizes into a high temperature and high pressure (1~10 GPa) plasma. This plasma induces shock waves during expansion from the irradiated surface, and mechanical impulses are transferred to the target. If the plasma is not confined, i.e., in open air, the pressure can only reach several tenths of one GPa. If it is confined by water or other media, the shock pressure can be magnified by a factor of 5 or more compared with the open-air condition [6]. At the same time, the shock pressure lasts 2 to 3 times longer than the laser pulse duration. In most LSP a coating is used to protect the target from thermal effects so that nearly pure mechanical effects are induced. The coating could be metallic foil, organic paints or adhesives. These coatings can modify the surface loading transmitted to the substrate by acoustic impedance mismatch effects at the coating-substrate interface, and an additional 50 percent increase in the peak stress values can be achieved [3]. Pressures above 1 GPa are above the yield stress of most metals, thus plastic deformation can be induced. As a result, if the peak shock pressure is over the *HEL* (Hugoniot Elastic Limit) of the target material for a suitable time duration, compressive stress distribution in the irradiated volume can be formed [2].

2.1 Shock Pressure. Earlier modeling work on laser-induced shock waves was carried out by Clauer et al. [2]. Their model considered the nonlinear coupled radiation and hydrodynamic equations governing pressure evolution at the metal surface during laser irradiation. Fabbro et al. [7] developed a model, which assumes that the laser irradiation is uniform and therefore shock propagation in the confining medium and the target as well is one-dimensional. This model was extended and analytical relationships for plastified depth and superficial residual stresses were given [8]. The 1-D assumption is appropriate when the size of laser beam, which typically follows a Gaussian distribution, is relatively large. The shock model in this paper made modifications to Fabbro's model to satisfy the special requirements of micro scale laser shock processing. The 1-D assumption is followed but a 2-D equivalence is considered to account for the small laser spot size. Figure 1(a) illustrates the shock model used in this paper. When plasma is formed at the interface of the solid and confining medium, its volume expands, its pressure increases and

Contributed by the Manufacturing Engineering Division for publication in the JOURNAL OF MANUFACTURING SCIENCE AND ENGINEERING. Manuscript received Nov. 2000; Revised July 2001. Associate Editor: S. G. Kapoor.

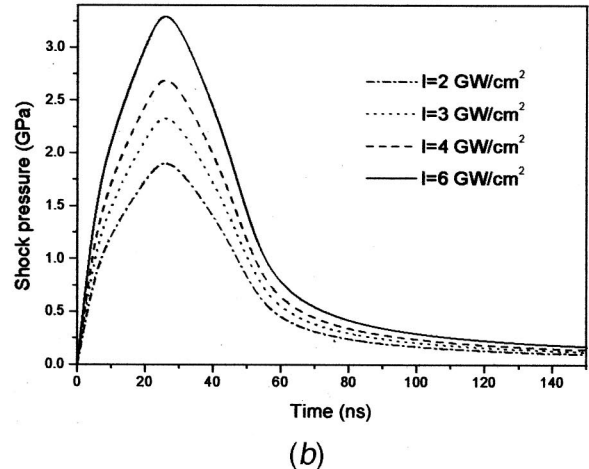
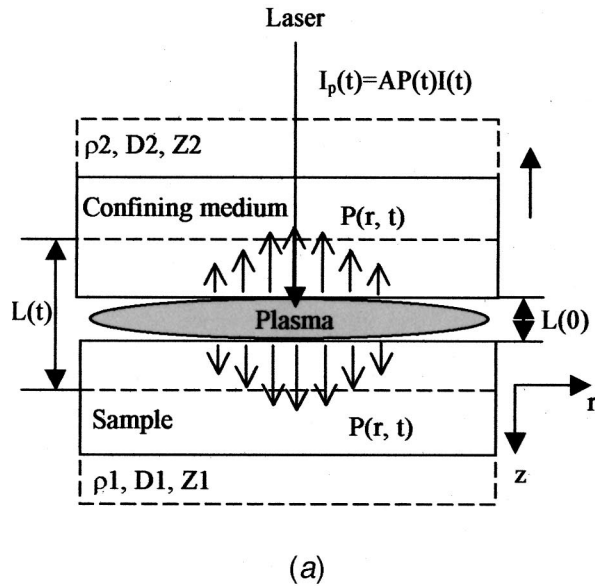


Fig. 1 (a) Modeling of laser shock processing (axisymmetry about the z-axis is assumed; and (b) effects of laser intensity on shock wave pressure (laser pulse duration is 50 ns, interaction coefficient $\alpha=0.2$, open air, and temperature $T=300$ K)

shock waves propagate into the sample and the confining medium. A portion of the incident laser intensity $I(t)$ is absorbed by the plasma as

$$I_p(t) = AP(t)I(t) \quad (1)$$

where $AP(t)$ is the absorption coefficient and t is time (Fig. 1(a)). Shock wave impedance is expressed as $Z_i = \rho_i D_i$, $i=1,2$, where ρ is density and D is the shock propagation velocity. The subscripts, 1 and 2, denote the solid target material and the confining medium, respectively. For instance, the impedance of copper is 4.18×10^7 kg/m²s, and the impedance of water is 1.65×10^6 kg/m²s [9]. Defining $Z = 2/(1/Z_1 + 1/Z_2)$ and assuming a constant fraction α of internal energy be used to increase the thermal energy of the plasma, the following relations between shock pressure $P(t)$ and plasma thickness $L(t)$ can be derived [7]:

$$\frac{dL(t)}{dt} = \frac{2P(t)}{Z} \quad (2)$$

$$\left(\frac{Z}{2} + \frac{3}{4\alpha}\right) \left(\frac{dL(t)}{dt}\right)^2 + \frac{3Z}{4\alpha} L(t) \frac{d^2L(t)}{dt^2} = I_p(t) \quad (3)$$

If $I(t)$, $AP(t)$ and α are constants, shock pressure is found to be proportional to the square root of laser intensity. If $I(t)$, $AP(t)$ and α are variables, the peak shock pressure is still proportional to the square root of the peak laser intensity and α . Thus it is reasonable to assume that shock pressure follows a Gaussian spatial distribution with its $1/e^2$ radius proportional to the $1/e^2$ radius of the laser beam. In this way, spatial nonuniformity of shock pressure is considered, which is needed when the laser spot size is small as in this case. The spatially uniform shock pressure $P(t)$ relates to the spatially nonuniform shock pressure as

$$P(r,t) = P(t) \exp\left(-\frac{r^2}{2r_0^2}\right) \quad (4)$$

where r is the radial distance from the center of the laser beam, and r_0 the radius of laser beam. $P(r,t)$ can be solved numerically from the above equations given initial values of $P(t)$ and $L(t)$. The values of $P(r,t)$ are then used as dynamic shock load in the stress analysis. Dependence of shock pressure on laser intensity is

shown in Fig. 1(b) where the laser intensity varies from 2 to 6 GW/cm² while α is kept as 0.2 and the pulse duration is kept as 50 ns.

2.2 Stress Analysis. In LSP, the target is subjected to very strong shock pressures (>1 GPa), the interaction time is very short (<100 ns), and the strain rate is very high ($>100,000$ s⁻¹). A review of constitutive equations for such high strain rates was given by Meyer [10]. The simplest model to describe the work hardening behavior of metals is $Y = A + B\varepsilon^n$, where Y is the yield strength, n , A and B are material constants, and ε is the equivalent plastic strain. The work hardening model was extended in Johnson's model [11] to include the influence of temperature T and strain rate $\dot{\varepsilon}$. Johnson's model was based on experiments with strain rates from 0 to 400 s⁻¹ and it did not consider pressure effects, which are very important in laser shock processing. A constitutive model applicable to ultrahigh pressures was given by Steinberg et al. [12]. Steinberg's model did not consider rate dependent effects, however. It was found that rate dependent effects played a minor role at pressures above 10 GPa and their rate independent model was verified to successfully reproduce shock experimental data in this range. But for shock pressures below 10 GPa, the rate dependent effects cannot be neglected. In laser shock processing, the pressure involved is fairly high (>1 GPa) but less than 10 GPa.

For laser shock processing, therefore, both the strain rate effects and ultrahigh pressure effects on material yield stress need to be considered. Based on the above mentioned models and assuming that the material compression is negligible in the range of working pressure (below 10 GPa), the following constitutive equations are suggested and used in this paper.

$$G = G_0 \left[1 + \left(\frac{G'_p}{G_0}\right) P + \left(\frac{G'_T}{G_0}\right) (T - 300) \right] \quad (5)$$

$$Y = Y_0 [1 + C \ln \dot{\varepsilon}] [1 + B\varepsilon]^n \left[1 + \left(\frac{Y'_p}{Y_0}\right) P + \left(\frac{Y'_T}{G_0}\right) (T - 300) \right] \quad (6)$$

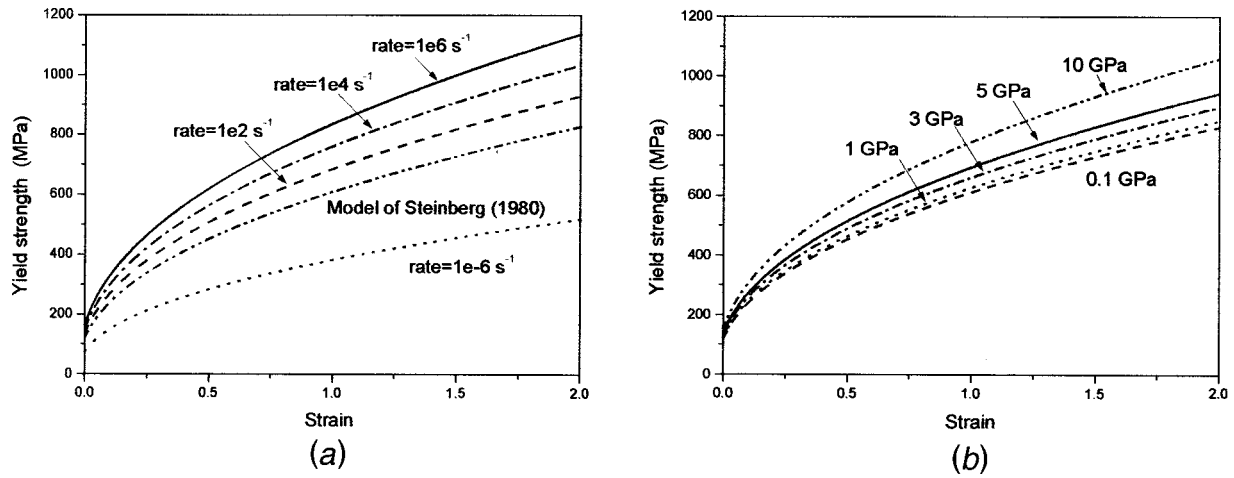


Fig. 2 (a) Influence of strain rate on the yield strength of copper (open air and temperature $T=300$ K); and (b) influence of shock pressure on the yield strength of copper (strain rate= 1 s^{-1} and temperature $T=300$ K)

$$G'_p = \frac{dG}{dP}, \quad G'_T = \frac{dG}{dT}, \quad Y'_p = \frac{dY}{dP}, \quad \frac{Y'_p}{Y_0} \approx \frac{G'_p}{G_0} \quad (7)$$

where G is the shear modulus, P is pressure, T is temperature, Y_0 and G_0 are values at reference state ($T=300$ K, $P=1$ atm, strain free), C is the logarithmic rate sensitivity at strain rate 1 s^{-1} , ε is strain, $\dot{\varepsilon}$ is strain rate, B and n are material parameters describing work hardening effect.

Figure 2(a) illustrates the increase of yield strength with strain rate for copper at $P=1$ atm and $T=300$ K. It is clear from this figure that rate dependence is strong for the kind of strain rates experienced in LSP. The yield strength increased by 37.3 percent at a strain rate of 10^6 s^{-1} as compared with the Steinberg's model. Figure 2(b) shows the influence of ultrahigh pressure on the yield strength of copper. Below 0.1 GPa, the influence of pressure is negligible. Obvious increase of yield strength with pressure starts at around 1 GPa (2.8 percent), and the yield strength increased 14 percent at 5 GPa and 28 percent at 10 GPa. For copper, the increase of yield strength from shock pressure effects is less important than but still comparable to that from strain rate effects in the range of 1 GPa to 5 GPa. For this reason, neither shock pressure effects nor strain rate effects can be neglected in stress analysis of laser shock processing.

In the following stress analysis, work hardening, strain rate and pressure effects on yield strength are considered while temperature is taken as room temperature. This is reasonable because only the coating is vaporized and minimal thermal effects are felt by the sample. Shock pressure is computed and used as loading for the 2D axisymmetric stress analysis. A commercial FEM code, ABAQUS, is used to compute the deformation and stress distribution of the sample under the shock pressure. The computation domain is 90 microns in z -direction and 1000 microns in r -direction (Fig. 1(a)) with 50 and 92 grids in each direction. The mesh is denser near the center and the top. The simulation is a dynamic implicit nonlinear process. Single and multiple pulses at single and multiple locations are simulated. The boundary conditions for the axisymmetric stress model are as follows. At the centerline, $d_r=0$ due to symmetry where d_r is the r -axis displacement; at the outer edge, traction free, that is $\sigma_{ij}n_j=0$, $i, j=r, z$; at the bottom surface, fixed in position, that is, $d_z=0$, $d_r=0$ and d_z is the z -axis displacement; and at the top surface, surface traction equals the applied shock pressure, that is, $\sigma_{ij}n_j=P(r,t)$, $i, j=r, z$.

3 Experiments

Copper foil of 90-micron thickness was used as samples. The sample was adhesively attached to a stainless back for rigid support and easy handling. The samples were polished and the sample size was about 10 mm square. To apply the coating, a thin layer of high vacuum grease (about 10 microns) was spread evenly on the polished sample surface, and the coating material, aluminum foil of 16 microns thick, which was chosen for its relatively low threshold of vaporization, then tightly pressed onto the grease. The sample was placed in a shallow container filled with distilled water around 3 mm above the sample. A frequency tripled Nd:YAG laser in TEM₀₀ mode was used, the pulse duration was 50 ns, and pulse repetition rate could vary between 1 Hz to 20 KHz. Laser beam diameter is 12 microns. Pulse numbers were varied from 1 to 6 at 1 KHz repetition rate, and pulse energy was varied from 160 μJ to 240 μJ corresponding to laser intensity of 2.83 to 4.24 GW/cm^2 . After shock processing, the coating layer and the vacuum grease were manually removed. The geometry of the shocked area was observed and measured using optical microscope, SEM and profilometer.

Besides geometry comparison, it is highly desirable to directly compare the experimental results of strain/stress distributions of the shocked area with that of simulations. Traditional X-ray diffraction measurement, however, is limited by its spatial resolution (~ 1 mm) and cannot be used directly to measure the micron scale strain distributions. Experiments were carried out, in which an array of equally spaced locations on a sample is consecutively shocked by laser pulses. It is termed as overlapped laser shock processing. The purpose of this type of experiments is twofold. First, traditional X-ray diffraction will have adequate spatial resolution to measure the average strain in the shocked region and this will provide indirect validation of the simulation results. Second, the overlapped laser shock processing is of interest in its own right when a shock-processed region of an arbitrary shape and area can be formed by overlapping shock processed locations. Spacing between neighboring shocked locations was 50.8 and 76.2 microns. Cu- $K\alpha$ X-ray source with a spot size of 2 mm by 2 mm and θ - 2θ symmetric configuration were used to measure strains in samples that underwent the overlapped LSP mentioned above. The strains in the z -direction (in-depth direction) were measured using Cu (111) and Cu (311) diffraction. The X-ray diffraction spectra of samples with the 50.8 and the 76.2 microns spacing were recorded. The unprocessed copper was also measured and used as reference in strain computation. The in-depth

strain E_z is calculated according to Bragg's law, $E_z = (d - d_0)/d_0 = (\sin(\theta_0)/\sin(\theta)) - 1$, where d is the lattice spacing of shocked area, d_0 the lattice spacing of the unprocessed area, θ the angle of spectral peak for shocked area and θ_0 the angle for the unprocessed area. The measurement results were used to further validate simulation results.

4 Results and Discussions

4.1 Strain Distributions. Figure 3(a) and (b) show a typical simulation result of radial strain $E_{11}(E_r)$ and the in-depth strain $E_{22}(E_z)$, respectively. Both are total strains that consist of elastic and plastic strains. For laser shock processing of copper, plastic strains are dominant. Deformation (dent) is clearly seen on the top surface near the centerline. As shown in Fig. 3(b), the maximum compressive strain of E_{22} occurs 10 microns below the top surface along the centerline, and the region of compressive strain expands from this point. On the top surface, a very thin layer of about 2 microns of tensile strain is observed. When the shock wave is acting on the sample, the material beneath the shocked area undergoes both plastic and elastic deformations. The shock pressure is attenuated as it propagates downwards and outwards. When the shock wave reaches the bottom, it is bounced back. The upward and downward shock pressure cancel each other. This explains the flat shape of the contour lines near the bottom. When the shock pressure is over, the top surface becomes traction free and stress relaxation occurs. The plastic deformation induced compressive strain under the top surface adjusts itself and finally balances the relaxation effects. This explains why the maximum compressive strain is not on the top surface. The radial strain (Fig. 3(a)) is tensile in the region where the in-depth strain is compressive. This is understandable because the material is isotropic and the in-depth strain will cause an in-plane (x - y) strain in the opposite sign under the principle of constant volume. The depth of plastic deformation reached about 70 microns in the sample of 90 microns thick. The simulation results were indirectly validated in the following geometry comparison.

4.2 Geometry Comparison Between Simulations and Experiments. In LSP, the metallic targets experience shock pressures exceeding their dynamic yield strength, thus plastic deformation is induced. In this paper, the aluminum coating layer protected the target from thermal effects so that nearly pure mechanical effects were induced. These were verified by experimental results in which smooth dents were formed but no signs of melting, burning, or ablation were observed. Figure 4 shows a

typical SEM micrograph of dents on copper surface. Each dent was produced by 3 laser pulses with pulse energy of $240 \mu\text{J}$ ($I = 4.24 \text{ GW/cm}^2$). Laser pulse duration is 50 ns, pulse repetition rate 1 KHz, beam diameter 12 microns, and laser wavelength 355 nm. The copper sample is 90 microns in thickness. The dents are quite visible under the SEM and are evidence of strong plastic deformations in LSP. The extent of the dents is about 50 microns.

The geometry of the dents was measured using a profilometer and compared with simulation results. As seen from Fig. 5, the simulated profiles generally agree with the experimental results quite well under different pulse energy levels and number of pulses. Discrepancies are seen at the edge of the dents. Experimental measurements show a larger radius at the edge. This is perhaps due to the fact that the simulation model assumes the shock waves propagate only in the vertical direction in the confining medium while in reality they do have 3D propagation effects.

Figure 6 shows further comparison between experiments and simulations in terms of dent depth and slope angle. The dents induced by shock waves are quite shallow and have a smooth transition onto the un-dented surface. This makes it difficult to define and measure the width of the dents. Instead of using width to characterize the profile, the angle (termed slope angle) between the surface normal and the tangential line of the middle part of the dent profile was used. As seen, the experimental results agree with simulation predictions. The relatively large deviations at 5 to 6 pulses were due to thermal effects because the coating layer was too thin to totally isolate the thermal effects when the number of pulses increases. As the pulse number increases from 2 to 6 the dent depth increases almost linearly (Fig. 6(a)). This is because the deformation is very small and each subsequent pulse sees almost the same geometry on the target as previous ones. On the other hand, when the pulse energy increases the dent depth accelerates (Fig. 6(b)). This is because when the pulse energy increases, both the level of shock pressure and the duration of the pressure increase as seen in Fig. 1(b). The general trends of slope angle in Fig. 6(a) and (b) can be similarly explained.

4.3 Transient Processes in Laser Shock Processing. The transient processes in laser shock processing, such as the evolution of acceleration, velocity, displacement, strain rate, plastic strain, etc., were studied. Strain rate effects are important for stress/strain analysis in laser shock processing. Figure 7(a) shows the evolution of strain rate of points along the centerline of the shock. The center point on the top surface is $(r, z) = (0, 0)$. The negative (compressive) strain rate in the z -direction reversed sign

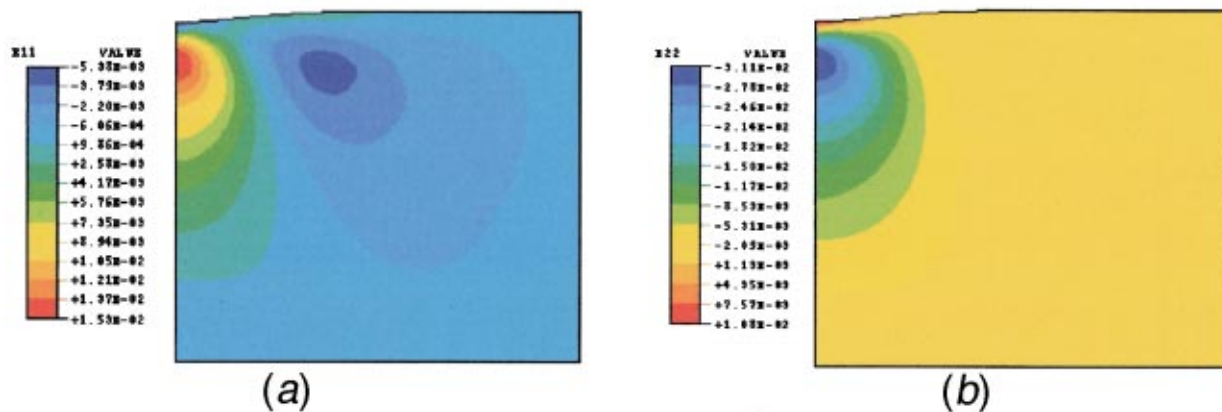


Fig. 3 Typical distribution of total strain at the end of a shock pulse (a) radial strain E_{11} ; and (b) in-depth strain E_{22} . Pulse energy $E = 240 \mu\text{J}$ ($I = 4.24 \text{ GW/cm}^2$), beam diameter is 12 microns, plasma absorption coefficient $AP = 0.545$ and interaction coefficient $\alpha = 0.2$. Axisymmetry is assumed. Computation domain is 90 microns by 1000 microns, and the region shown is 90 microns (z -direction) by 100 microns (r -direction) for clear view of the results. Deformation in the dented region is magnified by a factor of 3 for viewing clarity.

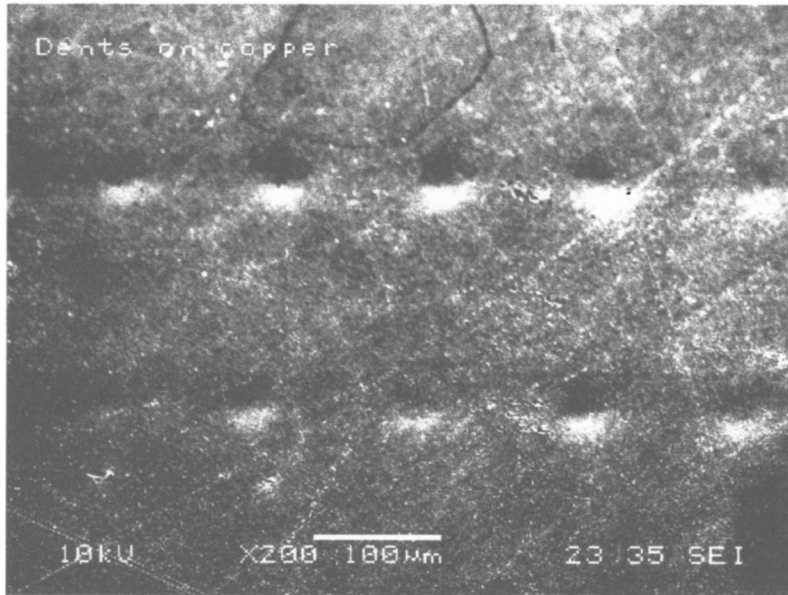


Fig. 4 SEM micrograph of dents on copper sample produced by laser shock processing (3 laser pulses at each location with each pulse energy $E = 240 \mu\text{J}$, laser pulse duration=50 ns, pulse repetition rate=1 KHz, beam diameter=12 microns, laser wavelength=355 nm, copper sample thickness=90 microns)

between 30 to 40 ns before reaching a peak. This timing is coincident with that required for the wave to propagate and reflect within the target material although shock wave is attenuated as time and distance increase. Shock waves travel in copper at 4700 m/s. The strain rates varied between -1.3×10^6 to $8 \times 10^5 \text{ s}^{-1}$ which could cause the yield strength of copper to increase by more than 30 percent.

Figure 7(b) shows the strain rates of three points on the top surface and two points inside the sample. The strain rates of the three top surface points are almost synchronized, and the amplitude decreases as they go farther away from the center. It can be seen that the two internal points (10, -10) and (30, -40) also have nearly synchronized transient strain rate evolutions with point (0, -10) and (0, -40) as shown in Fig. 7(a). The shock load applied on the top surface is the Gaussian spatial modulation of the 1D shock pressure (Eq. (4)), while the propagation of the shock wave

inside the sample is not restricted. The synchronization of the z-direction transient processes at the same height in the early stages indicates that the divergence of shock wave propagation is small, but the shock wave does spread out three-dimensionally as time and distance increase.

As seen, appreciable plastic strain occurs at around 9 nanoseconds. It increases rapidly from 10 to 60 nanoseconds. This is the period when the shock pressure is larger than the *HEL* (Hugniot Elastic Limit) of the material. Plastic strains reached a stable value after 200 nanoseconds, and the maximum plastic strain is 0.0322 at (0, -10). Note the pulse duration used here is 50 ns. To induce sufficient plastic deformations, pulse duration used in laser shock processing cannot be too short. Usually pulse duration longer than 20 nanoseconds is used. Pulse duration cannot be too big, either. A too large pulse duration may lead to serious thermal effects and too large deformations. For the above reasons, pulse

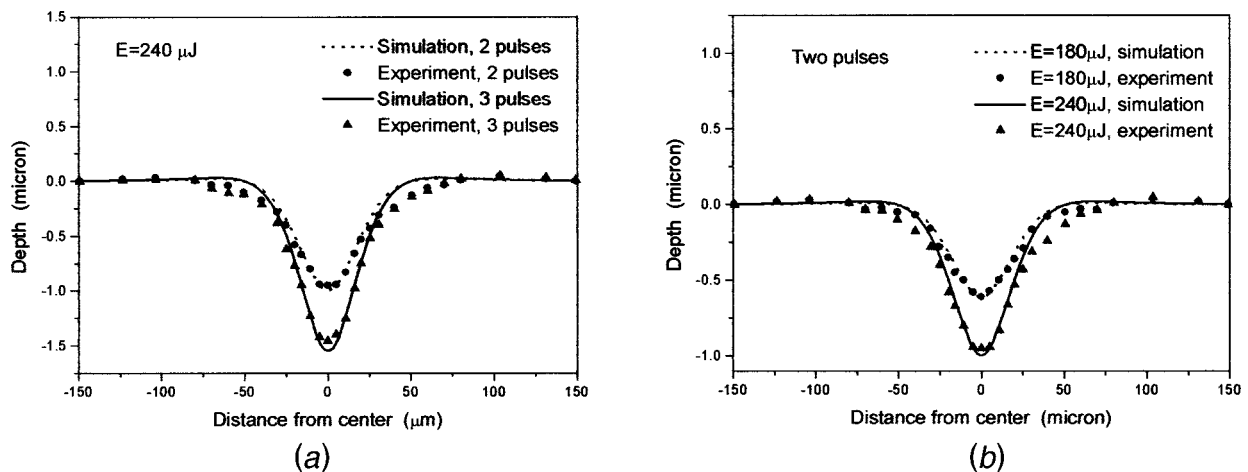


Fig. 5 Comparison of measured and simulated dent profiles (a) $E=240 \mu\text{J}$, 2 and 3 pulses; and (b) 2 pulses at $E=180 \mu\text{J}$ and $E=240 \mu\text{J}$. Laser beam diameter is 12 microns, pulse duration is 50 ns, pulse repetition rate is 1 KHz, plasma absorption coefficient $AP=0.545$, and interaction coefficient $\alpha=0.2$. Copper sample thickness=90 microns.

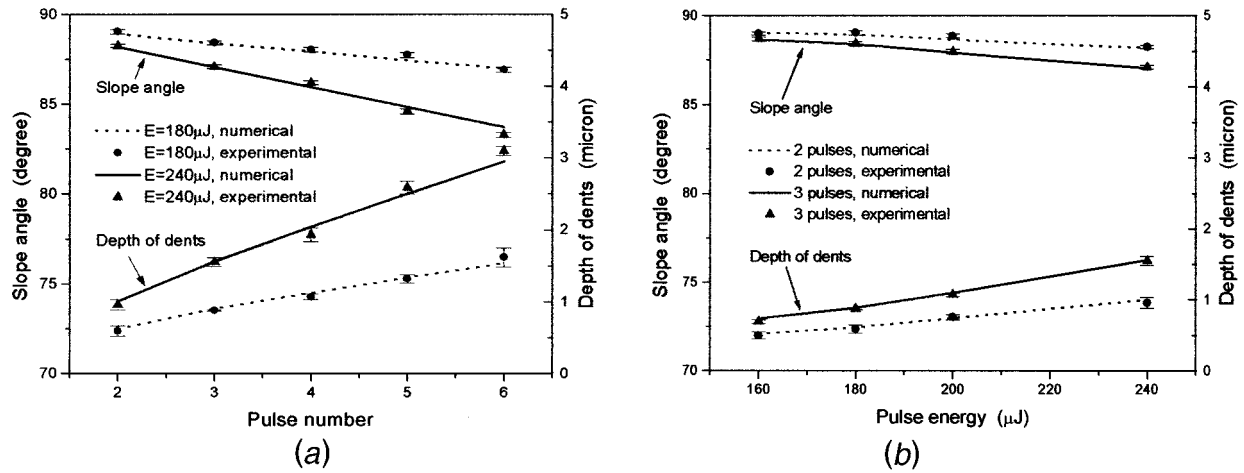


Fig. 6 Geometry comparison between experiments and simulations (a) dent slope angle (left axis) and dent depth (right axis) vs. pulse number, $E=180 \mu\text{J}$ and $240 \mu\text{J}$; and (b) dent slope angle (left axis) and dent depth (right axis) vs. pulse energy, pulse number=2 and 3. $AP=0.545$, and $\alpha=0.2$. Copper sample thickness=90 microns.

duration used in shock processing is normally shorter than 60 nanoseconds and longer than 20 nanoseconds for copper.

4.4 Overlapped LSP and X-ray Diffraction Measurements. Overlapped LSP was experimentally carried out to produce larger shocked areas and to overcome the limitation of spatial resolution of conventional X-ray diffraction. The 2D strains from simulations are first averaged along the depth direction corresponding to specific lattice planes to be examined in the X-ray diffraction. The strain values expressed in the cylindrical coordinates (r, z) at each shocked location are then transformed into Cartesian coordinates. Assuming individual shocks are independent, the strains at various shocked locations on the sample are finally summed up to obtain averaged strain map for the overlapped LSP, which is used to compare with the X-ray diffraction measurements. The process is described below.

4.4.1 Averaging Elastic Strains Along the Depth Direction. Since there exists a strain gradient in the in-depth direction, the spacing d between lattice planes and thus the strains obtained by the X-ray beam will be the average of this gradient over the effective penetration distance of X-rays, τ [13]. For θ - 2θ diffraction configuration, the effective penetration depth is:

$$\tau = \frac{\sin(\theta)}{2\mu} \quad (8)$$

where μ is the X-ray absorption coefficient of the sample. For Cu- $K\alpha$ X-ray beam, μ of copper is 460.25 cm^{-1} . The average strain over the total sample depth H can be expressed as [13]:

$$\varepsilon(r) = \frac{\int_0^H \varepsilon(r, z) \exp\left(-\frac{z}{\tau}\right) dz}{\int_0^H \exp\left(-\frac{z}{\tau}\right) dz} \quad (9)$$

Using Eqs. (8) and (9), the 2D strain distribution $\varepsilon(r, z)$ of the axisymmetric simulation is averaged to obtain $\varepsilon(r)$. In order to sum up the strains induced at individual shocked locations, $\varepsilon(r)$ is converted from cylindrical coordinates to Cartesian coordinates via

$$E_{xyz} = Q^* E_{cyl} * Q' \quad (10)$$

where E_{xyz} is the strain tensor in Cartesian coordinates and E_{cyl} the strain tensor in cylindrical coordinates and takes the form of

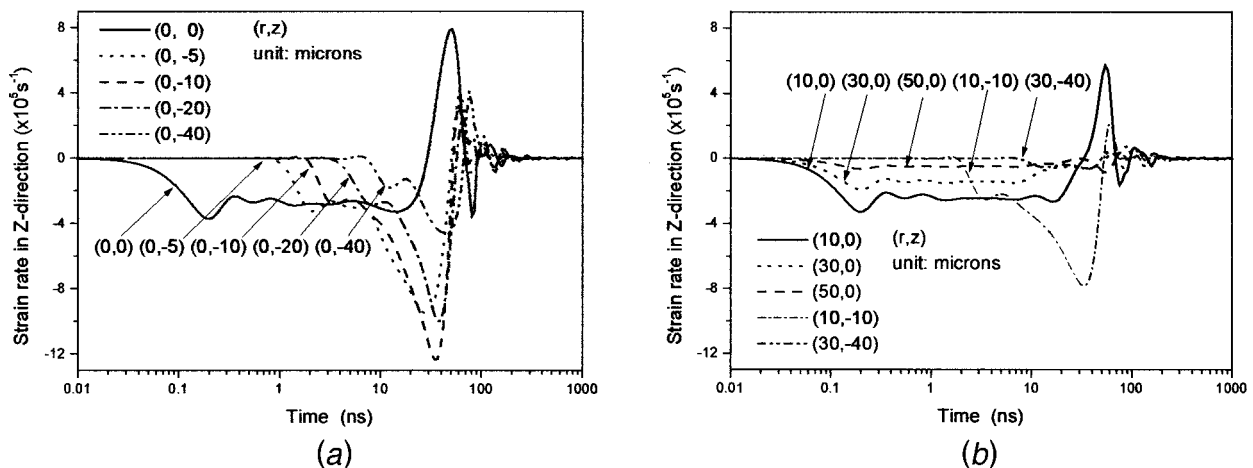


Fig. 7 Evolution of strain rate in z-direction (in-depth direction) (a) strain rate of points on the centerline; and (b) strain rate of points along the surface and at other locations. (r, z) gives the location of a point, and $(0, 0)$ is the center point on the top surface. Single pulse, $E=240 \mu\text{J}$, $AP=0.545$, and $\alpha=0.2$.

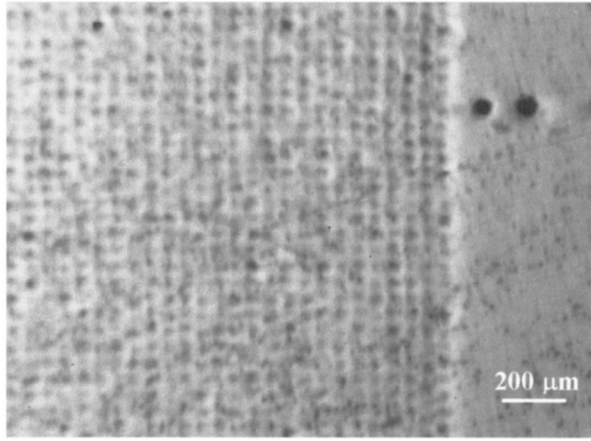


Fig. 8 Typical optical micrograph of dented region (left) produced by laser shock processing at an array of equally spaced locations, spacing=50.8 microns. $E=240 \mu\text{J}$, 2 pulses at each location, beam diameter=12 microns. The region on the right of the graph is unprocessed, original copper surface, on which holes were laser drilled to assist observation and positioning in subsequent X-ray diffraction measurements.

$$E_{cyl} = \begin{bmatrix} \varepsilon_{rr} & \varepsilon_{r\theta} & \varepsilon_{rz} \\ \varepsilon_{r\theta} & \varepsilon_{\theta\theta} & \varepsilon_{\theta z} \\ \varepsilon_{rz} & \varepsilon_{\theta z} & \varepsilon_{zz} \end{bmatrix} \quad (11)$$

The 2D axisymmetric constraints require $\varepsilon_{\theta z}$ and ε_{rz} to be zero. The coordinate transformation matrix Q is

$$Q = \begin{bmatrix} \cos(\phi) & -\sin(\phi) & 0 \\ \sin(\phi) & \cos(\phi) & 0 \\ 0 & 0 & 1 \end{bmatrix} \quad (12)$$

where ϕ is the rotational angle. Q' is the transpose of matrix Q .

4.4.2 Comparison of Simulation and X-ray Diffraction Results. Figure 8 shows an optical micrograph of the copper sample shock processed by overlapping laser pulses. The overlap spacing is 50.8 microns. The left side is the dented region and the right side is the unprocessed, original copper surface. Holes were drilled on the unprocessed region to assist locationing in subse-

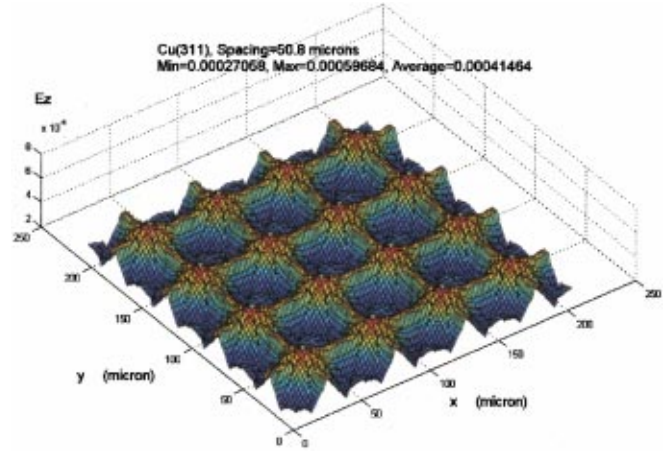
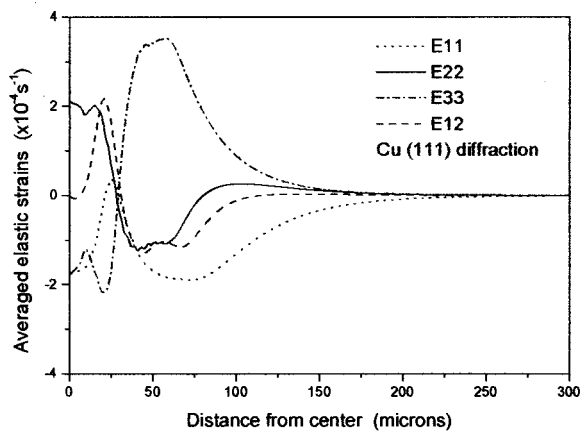


Fig. 10 Overlapping results of the depth-direction elastic strain Ez ($E22$) for comparison with subsequent X-ray diffraction measurement of Cu(311), spacing=50.8 microns. Two pulses at each location, $E=240 \mu\text{J}$, $AP=0.545$, and $\alpha=0.2$.

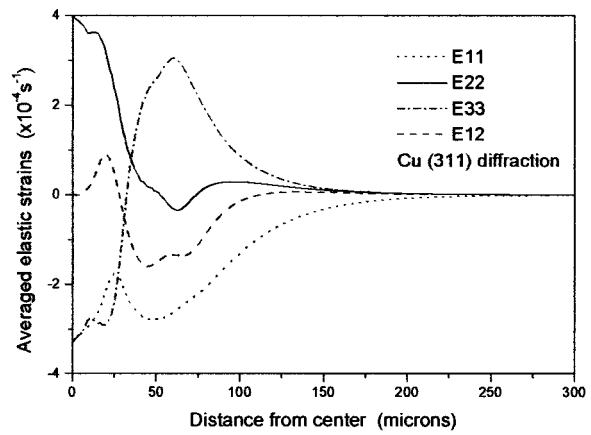
quent X-ray diffraction measurements. The grain size of the copper sample is between 10 to 15 microns, and the grains are randomly oriented. For such grain sizes, a 2 mm by 2 mm X-ray beam covers a large number of grains.

Figure 9 shows the elastic strains averaged along the depth direction at a single shocked location according to Eq. (9). Figure 9(a) is averaged according to the effective penetration depth of Cu (111) diffraction, that is, 4.0168 microns, while Fig. 9(b) is obtained according to the penetration depth for Cu (311) diffraction, which is 7.6931 microns. All four components of the strain tensor in cylindrical coordinates are shown, with $E11$ being in the radial direction (r) and $E22$ being in the depth direction (z). Because of the difference in effective penetration depth, the average results are different. The averaged in-depth elastic strains in the cylindrical coordinates are then expressed in terms of the Cartesian coordinates (Eq. (10)).

Figure 10 shows the in-depth strain maps resulting from summing up the Cu (311) averaged elastic strains (from Fig. 9(b)) but expressed in the Cartesian coordinates) of different shocked locations. The spacing is 50.8 microns. Only a 4 by 4 matrix of the shocked locations are shown, but it is representative of the entire



(a)



(b)

Fig. 9 Simulated elastic strains averaged along the depth direction in anticipation of comparison with subsequent X-ray diffraction measurement (a) for X-ray diffraction measurement of Cu (111); and (b) for X-ray diffraction measurement of Cu (311). Two pulses, $E=240 \mu\text{J}$, $AP=0.545$, and $\alpha=0.2$. $E11$ is in radial, $E22$ depth, and $E33$ circumferential direction.

Table 1 Comparison of X-ray diffraction measurements with simulation predictions

Diffraction plane and overlapping spacing (μm)	θ (Degrees)	θ_b (Degrees)	E_z (experiment, $\times 10^{-4}$)	E_z (simulation, $\times 10^{-4}$)
Cu (111), 50.8	43.5802 \pm 0.0004	43.5865 \pm 0.0005	1.4844 \pm 0.28	1.79
Cu (111), 76.2	43.5640 \pm 0.0004	43.5678 \pm 0.0003	0.8233 \pm 0.0858	0.8935
Cu (311), 50.8	90.1317 \pm 0.0019	90.1609 \pm 0.0020	2.5449 \pm 0.1619	4.1464
Cu (311), 76.2	90.1267 \pm 0.0032	90.1443 \pm 0.0020	1.5298 \pm 0.2820	1.9743

shocked region. The overlapping results of the averaged in-depth strain E_z are all tensile with the grand average being 4.1464×10^{-4} for the spacing of 50.8 microns. The averaged E_z is 1.9743×10^{-4} for the spacing of 76.2 microns (not shown). This results in compressive average strains of E_x and E_y assuming they are equal-biaxial and under the constant volume principle. It is observed that the elastic strains induced by overlapping at 50.8-micron spacing are about twice as large as that at 76.2-micron spacing, and the range of variation for 50.8 microns is smaller than that of 76.2 microns. So the overlapping spacing can be used to influence the values as well as the uniformity of the strain distribution. Because of the compressive average in-plane stresses as just mentioned above, it can be expected that large areas of compressive average in-plane residual stress distributions will be the result of the shock overlapping. Such in-plane compressive residual stress distribution is desired for the prevention of crack formation and propagation. Similar calculations were carried out for Cu (111) diffraction and for other strain components. The strain values of Cu (111) diffraction are smaller than the strain values of Cu (311) diffraction due to the fact that Cu (111) dif-

fraction is the average of a shallower top layer than Cu (311) diffraction, and the in-depth residual stress is close to zero near the top.

The averaged elastic strain E_z values are compared with the results from X-ray diffraction measurements as shown in Table 1. The X-ray diffraction spectra of the unprocessed sample and the shocked regions of 50.8-micron and 76.2-micron spacing were recorded. Measurements were repeated three times under each condition and the repeatability is indicated in Table 1 in terms of the standard errors. From Table 1 it is seen that X-ray measurement results show the same trends as the simulation predictions but are lower than the simulation predictions especially in case of Cu (311). The overestimation by the simulation is perhaps due to some of the assumptions made in the simulation and subsequent data processing. In simulation the strain contributions from neighboring locations were directly summed up, while in experiments the accumulation of strains is nonlinear due to work hardening effects. Energy dissipation into the coating layer was neglected in simulation, and the bottom surface was not absolutely fixed in position in experiments. All these factors lead to the overestima-

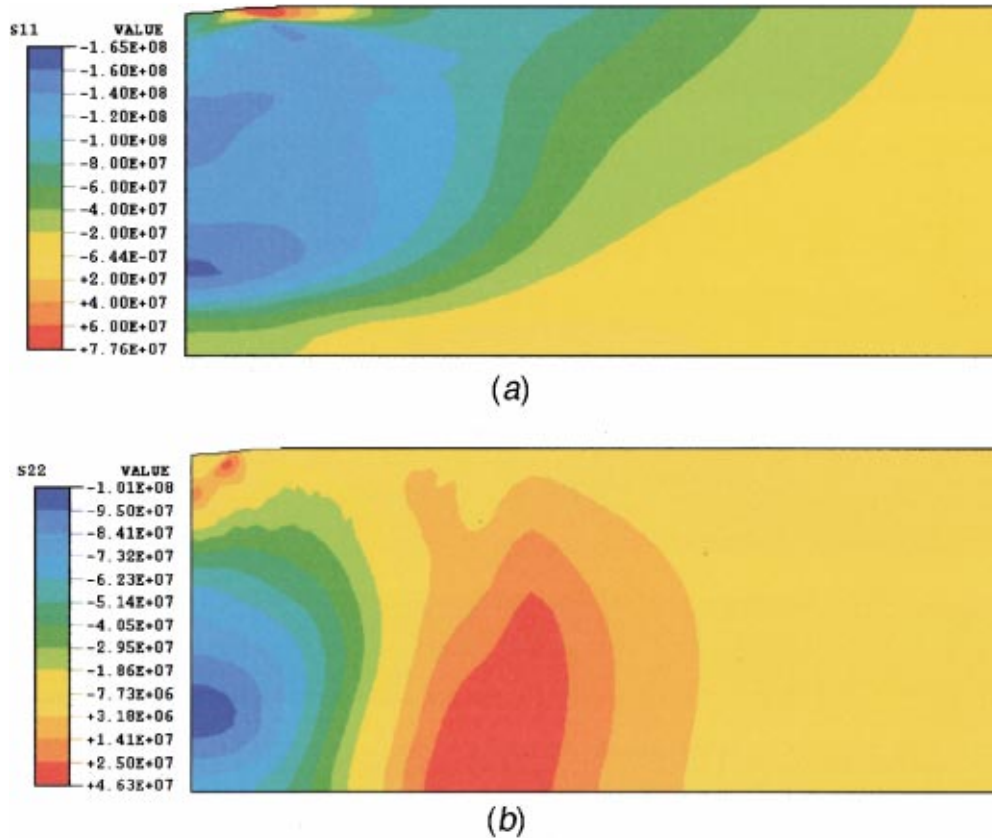


Fig. 11 Typical distribution of residual stresses (a) radial residual stress S_{11} and (b) in-depth residual stress S_{22} , $E = 240 \mu\text{J}$, beam diameter=12 microns. Stress unit: Pascal. Axisymmetry is assumed. Computation domain is 90 microns by 1000 microns, and the region shown is 90 microns by 200 microns for clear view of the results. Deformation in the dented region is magnified by a factor of 3 for viewing clarity.

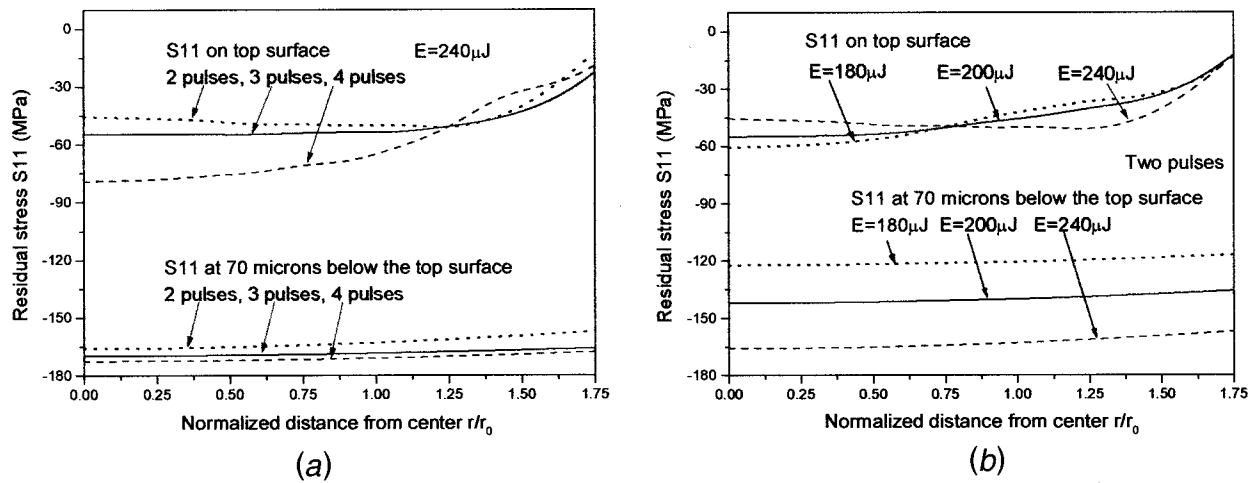


Fig. 12 Distribution of residual stresses on the top surface and at 70 microns below the top surface (a) radial residual stress S_{11} , $E=240 \mu\text{J}$, 2 to 4 pulses; and (b) radial residual stress S_{11} , 2 pulses, $E=180, 200$ and $240 \mu\text{J}$. Distance from the center is normalized to the radius of laser beam r_0 , where $r_0=6$ microns.

tion of simulation predictions, but the trends of variation agree with that measured by X-ray diffraction. Thus, in addition to the geometry comparison presented in an early section, this comparison further validates the simulation process. The residual stress distributions from simulations will be analyzed in the following section. It should be noted that using the conventional X-ray diffraction technique for micro scale measurements is not ideal. Its limited spatial resolution only allows measurements of strains averaged over an area. More recently reported work on X-ray microdiffraction techniques would be more suitable when they mature.

4.5 Residual Stresses. Figure 11 shows a typical distribution of residual stresses for a single pulse at the energy level $E=240 \mu\text{J}$. The computation domain is 90 microns by 1000 microns, and the region shown is 90 microns by 200 microns for clear view of the results. As seen from Fig. 11(a), radial stress S_{11} is compressive in a wide region below the top surface with the maximum of 165 MPa reached along the centerline and about 70 microns into the sample. On the top surface, S_{11} is compressive within 10 microns from the center and is tensile in the range of 10 to 38 microns, and then becomes compressive again. Such tensile radial stress near the edge of laser irradiation was also observed in LSP using large beam sizes [2]. This thin layer (about 2.5 microns deep) of tensile stress is undesirable, but it may be altered by overlapping laser pulses at proper spacing, as illustrated in Section 4.4. The wide range of compressive radial stress distribution near the top surface is desired for the prevention of crack formation and propagation. Figure 11(b) shows the distribution of in-depth residual stress S_{22} . S_{22} is close to zero near the top surface as expected from the equilibrium requirement, and becomes compressive at the lower center part of the sample. The locations of the maximum tensile and compressive in-depth residual stresses are close to the bottom surface instead of the top surface. One explanation is that the bottom surface is fixed in position, while the top surface is traction free when the shock load is removed. The top part of the sample will have nearly zero in-depth stress after sufficient stress relaxation, but the center bottom part cannot relax as the top surface does because both the centerline and the bottom surface are fixed in position. As a result, the in-depth residual stress accumulates near the center bottom region.

Figure 12 illustrates the distribution of residual stresses on the top surface and at 70 microns below the top surface. The distance from the center is normalized to the radius of laser beam r_0 , where $r_0=6$ microns. Stress distribution within $1.75 r_0$ was shown to view the laser-irradiated region and its vicinity in detail.

Under all conditions, the radial stress S_{11} (equivalent to in-plane (x - y) stress if equal-biaxial is assumed) on the surface is compressive within the $1.75 r_0$ range and the compressive radial stress reaches around 160 MPa 70 microns below the top surface. When r/r_0 approaches 1.75 and is greater than 1.75 for that matter, the radial stress on the top surface rises and eventually becomes tensile (Fig. 11(a)), which is undesirable but may be alleviated by overlapping pulses at proper spacing as discussed in the previous paragraph. It is interesting to note that the radial stress S_{11} on the top surface is more sensitive to the number of pulses (Fig. 12(a)) while S_{11} deep below the top surface (70 microns) is more sensitive to the pulse energy level (Fig. 12(b)). It is easy to understand why S_{11} increases with the energy level below the top surface. Its insensitivity to the energy level at the top surface is due to the fact that relaxation took place near the top surface after the shock pressure is over, therefore regardless of the energy level, relaxation will always take place. As a result, S_{11} at the top surface seems less sensitive to the energy level. The same reasoning can be used to explain why the increase in the number of pulses causes appreciable increase in S_{11} at the top surface. The reason that S_{11} 70-microns below the top surface are less sensitive to the number of pulses is due to the work-hardening effect.

5 Conclusions

Laser shock processing at the scale of microns for the purpose of residual stress distribution alteration was discussed in this paper. A 2D axisymmetric model for shock pressure computation was given to account for the micro scale involved. A modified constitution relation taking into account of high strain rate, ultra-high pressure, temperature and work hardening effects were given. The model was experimentally validated in terms of geometry of the shock-dented area and the averaged in-depth strain. It is shown that for a laser beam of 6 microns in radius and pulse energy of $240 \mu\text{J}$, in-plane (x - y) compressive residual stress is imparted on the surface of copper samples within a region of about two radii of the laser beam, and over 150 MPa compressive stress is imparted 70 microns into the target material. A small region around the edge of the dented area is seen as tensile, which may be alleviated by overlapping laser pulses at proper spacing. It is shown that it is possible to impart desirable residual stress distributions into micro scale metallic components by properly choosing laser intensity, number of pulses and spacing. This paper shows that micro scale laser shock processing has the potential to alter the mechanical properties and thus improve fatigue performance of metallic MEMS components and devices. It may also be

combined with laser micromachining processes, which alone often leave an undesirable residual stress distribution in the machined components, to allow the net residual stress distributions in favor of improved fatigue life of the components.

Acknowledgments

Financial support from NSF under grant DMI-9813453 and equipment support from ESI are gratefully acknowledged. Guidance and assistance with X-ray diffraction by Prof. G. S. Cargill and Ms. Laura Roos (Lehigh University) are appreciated.

References

[1] White, R. M., 1963, "Elastic Wave Generation by Electron Bombardment or Electromagnetic Wave Absorption," *J. Appl. Phys.*, **34**, pp. 2123–2124.
[2] Clauer, A. H., and Holbrook, J. H., 1981, "Effects of Laser Induced Shock Waves on Metals," *Shock Waves and High Strain Phenomena in Metals-Concepts and Applications*, New York, Plenum, pp. 675–702.
[3] Peyre, P., Scherpereel, X., Berthe, L., and Fabbro, R., 1998, "Current Trends in Laser Shock Processing," *Surf. Eng.*, **14**, No. 5, pp. 377–380.
[4] Walraven, J. A., Mani, S. S., Fleming, J. G., Headley, T. J., Kotula, P. G., Pimentel, A. A., Rye, M. J., Tanner, D. M., and Smith, N. F., 2000, "Failure Analysis of Tungsten Coated Polysilicon Micromachined Microengines,"

MEMS Reliability for Critical Applications, Proceedings of SPIE, Vol. 4180, pp. 49–57.
[5] Frederick, Kevin M., and Fedder, Gary K., 2000, "Mechanical Effects of Fatigue and Charge on CMOS MEMS," *MEMS Reliability for Critical Applications, Proceedings of SPIE*, Vol. 4180, pp. 108–116.
[6] Fox, J. A., 1974, "Effect of Water and Paint Coatings on Laser-Irradiated Targets," *Appl. Phys. Lett.*, **24**, No. 10, pp. 461–464.
[7] Fabbro, R., Fournier, J., Ballard, P., Devaux, D., and Virmont, J., 1990, "Physical Study of Laser-Produced Plasma in Confined Geometry," *J. Appl. Phys.*, **68**, No. 2, pp. 775–784.
[8] Peyre, P., Fabbro, R., Berthe, L., and Dubouchet, C., 1996, "Laser Shock Processing of Materials, Physical Processes Involved and Examples of Applications," *J. Laser Appl.*, **8**, pp. 135–141.
[9] Assay, James R., and Shahipoor, Mohsen, 1992, *High-Pressure Shock Compression of Solids*, New York, Springer-Verlag, pp. 78–82.
[10] Meyer, L. W., 1992, "Constitutive Equations at High Strain Rates," *Shock-wave and High-Strain-Rate Phenomena in Metals*, Marcel Dekker, Inc., New York, pp. 49–68.
[11] Johnson, G. R., Hoegfeldt, J. M., Lindholm, U. S., and Nagy, A., 1983, "Response of Various Metals to Large Torsional Strain Over a Large Range of Strain Rates," *J. Eng. Mater. Technol.*, **105**, pp. 42–53.
[12] Steinberg, D. J., Cochran, S. G., and Guinan, M. W., 1980, "A Constitutive Model for Metals Applicable at High-Strain Rate," *J. Appl. Phys.*, **51**, No. 3, pp. 1498–1504.
[13] Noyan, I. C., and Cohen, J. B., 1986, *Residual Stress*, Springer-Verlag New York, Inc., New York, pp. 135.